ACADEMIC
PRESS

Transient response of a hydraulic engine mount

H. Adiguna[a], M. Tiwari[a], R. Singh[a],*, H.E. Tseng[b], D. Hrovat[b]

[a] Department of Mechanical Engineering, Acoustics and Dynamics Laboratory, Center for Automotive Research,
The Ohio State University, 206 West, 18th Avenue, Columbus, OH 43210-1107, USA
[b] Scientific Research Laboratory, Ford Motor Company, Dearborn, MI 48124, USA

Abstract

Linear and non-linear transient responses of a typical hydraulic engine mount are analytically and experimentally studied in this paper. First, a lumped parameter linear model is used to approximate the typical step response and to suggest parameters that must be experimentally determined. Various configurations as related to inertia track and decoupler are analyzed. Two bench experiments are constructed for the identification of non-linear compliances and resistances. One of the main non-linear characteristics, however, comes from the decoupler mechanism. To accurately predict the time events of the decoupler opening and closing, an equivalent viscous damper model is employed along with a multi-staged switching mechanism. Additionally, non-linear behavior arising due to the vacuum formation in the top chamber is studied by defining a bi-linear asymmetric stiffness curve. New transient experiments are conducted on an elastomer test system, and measured transmitted force and top chamber pressure signals are analyzed. Results of the proposed simulation model match well with measured responses when step up, step down and triangular waveforms are applied. Areas for future research are identified.
© 2003 Elsevier Ltd. All rights reserved.

1. Introduction

1.1. Motivation

Hydraulic mounts are designed and tuned to provide amplitude-sensitive and spectrally varying properties [1]. Such devices are increasingly being employed in many ground vehicles to isolate engines and transmissions. The performances of such hydraulic mounts are typically measured on a steady state basis using the sinusoidal non-resonant-type test methods [2] and regularly

employed for product design and quality control. Conversely, their transient characteristics are poorly understood, and the relevant simulation methods and experimental techniques are not readily available. Therefore, the chief objective of this article is to develop linear and non-linear models that may be utilized to design, specify and diagnose the transient characteristics arising due to many vehicle conditions such as travel on bumpy roads, abrupt accelerations or decelerations, braking, and cornering. In a recent paper, Nessler et al. [3] developed a roll down methodology to predict the driver's seat track response to garage shift events. They concluded that the response of a garage shift event at the seat track mounting is due primarily to vibration transmitted through the power train mounts. We will also propose new transient experiments and compare prediction and measurements for selected transients.

1.2. Literature review

There is a substantial body of literature on the steady state (sinusoidal) behavior of hydraulic mounts. Singh et al. [4] provide a comprehensive review of previous research on passive mounts. Further, they [4] developed a linear lumped parameter model, which after certain assumptions results in a simple transfer function model with second order numerator and denominator dynamics. Parametric design studies show the effects of top chamber compliance and inertia track geometry. The continuation of this work, presented in Ref. [5], resulted in a non-linear model that emphasizes the non-linearities due to decoupler and inertia track. However, only the kinematic switching mechanism was defined. Non-linear system parameters used in the model must be measured, as explained in Ref. [2]. Kim and Singh [5] also proposed an adaptive mount system that implements an on–off damping control mode. In Ref. [5], the performance of a two-degree-of-freedom hydraulic mounting system was compared with that of elastomeric mount system for base excited impulse and step displacement inputs to the mount.

Colgate et al. [6] suggested two linear, frequency domain models to distinguish between the small (<0.5 mm) and large (>0.5 mm) amplitudes of excitation. Their non-linear model, by means of piecewise and equivalent linearization, assumed that a squeeze film produces a damping force as the decoupler bottoms out. The steady state response to a composite excitation with two sinusoids of different amplitudes and frequencies was also studied. Royston and Singh calculate the vibratory power flow through a hydraulic engine mount into a resonant receiver by employing a dual domain strategy based on the Galerkin's method [7].

Based on the existing literature, it is clear that virtually no efforts have been made to analyze the transient behavior, with the exception of Kim and Singh [5] who studied mount in the context of a simplified model. Likewise, no experimental methods or data are available to the best of our knowledge [8,9].

1.3. Objectives and example case

The main objective of this study is to develop linear and non-linear models with emphasis on time domain issues, and to validate such models by comparing simulation with transient experiments. Since the mount exhibits multiple non-linearities, characterization of such a system requires a combined experimental and analytical strategy. In particular, our research focuses on the non-linear characteristics introduced by the vacuum in the top chamber, inertia track

dynamics, and the decoupler switching mechanism. New dynamic characterization tests are also conducted on an elastomer test system under step, triangular and sawtooth displacement waveforms.

The example case is schematically shown in Fig. 1. In practice, three or four mounts are used to support engines and transmissions, out of which one is typically the hydraulic mount. The device is mounted to the engine through the top mounting studs (1) and to the chassis through the bottom mounting studs (2). Metal inserts (3, 6) are molded into the elastomeric element (4) so that the compression and shear deformations of the elastomeric element provide stiffness to support the static engine weight. The pin (5) acts as a stopper for preventing excessive tension in the top chamber for very large tensile displacements. The top (7) and bottom (8) chambers are filled with anti-freeze and water mixture. Upon the compression of the top chamber, the liquid is forced to flow through the two fluid channels in the orifice plate (10). This consists of an inertia track (11), which is a long, narrow channel to provide the fluid damping, and a decoupler (12) with a wider orifice along with a free floating elastomeric disk. The flexible rubber diaphragm (9) acts like an accumulator as the fluid flows from the top to the bottom chamber. The air breather (13) allows the air to escape from the base plate (14). The most critical component is the orifice plate (10) since minor changes in its geometry and flow conditions could influence dynamic behavior in a significant manner. Even though only one mount is examined, various sub-sets are developed by modifying the internal components.
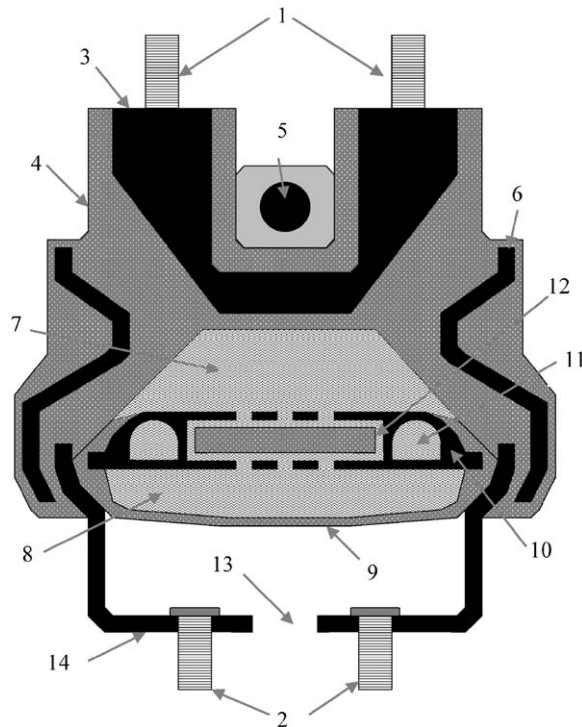

Fig. 1. Example case: hydraulic engine mount. Refer to Section 1.3 for the identification of components.

2. Analytical formulation and system parameters

2.1. Lumped parameter model

The hydraulic mount is modelled by lumping the fluid system into several control volumes as shown in Fig. 2. Our discretization strategy is consistent with low frequency oriented models that have been utilized before [4,10]. The system parameters are either calculated using theoretical formulas or experimentally measured. They include the top (#1) and bottom (#2) chamber fluid compliances (C_1 and C_2), elastomeric element stiffness (k_r) and damping (b_r), inertia track inertance (I_i), fluid resistance (R_i), and decoupler resistance (R_d). Through experimentation, it is shown that C_1, C_2, R_i, and R_d have non-linear characteristics. However, the largest contribution to the non-linear characteristics of the mount seems to come from the switching mechanism of the decoupler. It acts like an on–off valve since it is actuated by the pressure difference (p_1-p_2) between the top and bottom chambers. The concept of the hydraulic mount is illustrated in Fig. 3 where $u(x,t)$ is the hydraulic reaction force.

The momentum and continuity equations yield the following equations; refer to Refs. [4,10] for details:

$$q_i(t) + q_d(t) = A_p \dot{x}(t) - C_1(p_1)\dot{p}_1(t), \tag{1}$$

$$-q_i(t) - q_d(t) = C_2(p_2)\dot{p}_2(t), \tag{2}$$

$$F_T(t) = b_r \dot{x}(t) + k_r x(t) + A_p(\bar{p} - p_1(t)), \tag{3}$$

where q_i, q_d, p_1, p_2, $\bar{p}$, x, A_p, and F_T denote the flow rate through inertia track, flow rate through decoupler, top chamber pressure, bottom chamber pressure, pressure at static equilibrium condition, displacement excitation, equivalent piston area, and transmitted force, respectively.
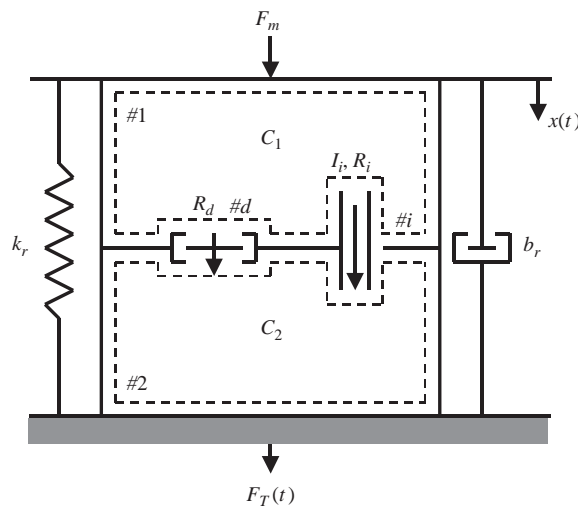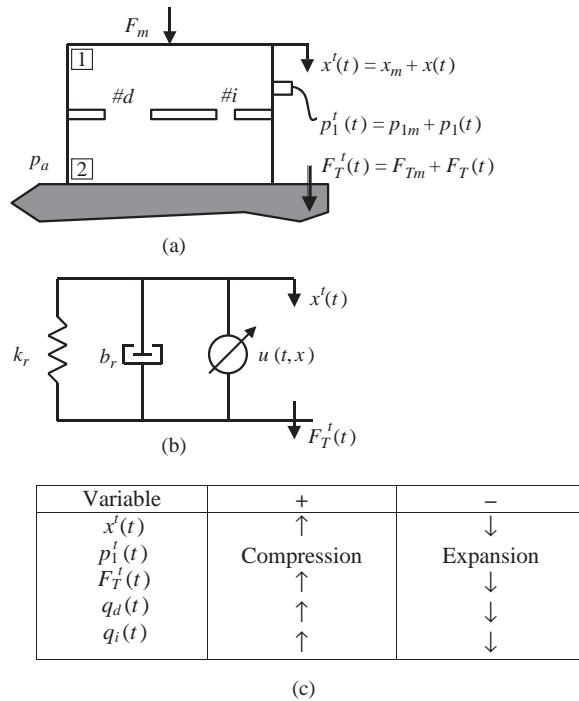

Fig. 2. Lumped parameter model.

Fig. 3. Hydraulic mount concept: (a) measured variables; (b) force transmission paths; and (c) sign convention where ↑ implies an upward motion and ↓ refers to the downward motion.

Engine mounts always operate at a given preload (F_m), which can be compressive or tensile depending upon the application. Typical preloads range from about 1200 to 2400 N for automotive applications. The dynamic excitation in the standard mount tests is usually specified by a harmonic displacement, $x(t) = X \sin(2\pi f t)$, where the amplitude X ranges from 0.05 to 1.5 mm and the frequency f in Hz depends on the application [11]. The output of interest is the force transmitted to the base, $F_T(t) = |F_T(t)| \sin(2\pi f t + \phi)$. In such tests, super- and sub-harmonics of f are ignored [8,11]. Unlike the conventional elastomeric mount, $F_T(t)$ in a hydraulic mount includes contribution from both elastomeric and fluid elements. While the elastomeric element may be considered linear, the fluid system could behave in a linear or non-linear manner depending upon the internal configuration of the mount and the amplitude of the excitation.

The orifice plate positioned between the top and bottom chambers controls the fluid system characteristics. As shown in Fig. 4, the top orifice plate holds the decoupler and provides the fluid channel for the inertia track. The bottom orifice plate provides the entrance/exit passages for the decoupler and inertia track as well as a mechanism for closing the top orifice plate so that no leaking occurs. Measured dimensions are listed in Table 1.

2.2. Inertia track

The inertia track of Fig. 4 is long and spiral, with a small cross-sectional area (A_i) channel. Due to its geometry, inertia track has high resistance (R_i) and inertance (I_i), which result in sufficiently
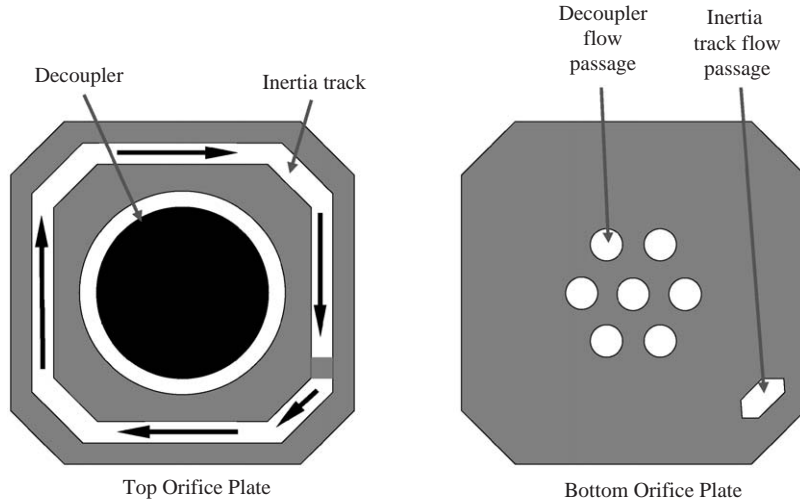
Fig. 4. Schematic of the orifice plate.

Table 1
Hydraulic mount parameters

(a) Measured orifice plate geometry
Inertia track:
Length (l_i) = 23.6 cm, cross-sectional area (A_i) = 84 mm^2
Decoupler:
Diameter (d_d) = 5 cm, area (A_d) = 1.96e-3 m^2, gap (δ_d) = 1.1 mm,
thickness (t_d) = 4 mm, holes area (H_d) = 1.22e-4 m^2

(b) Paramerters of the linear model
b_r = 0.5 N s/mm, k_r = 320 N/mm, C_1 = 2.5e-11 m^5/N, C_2 = 2.4e-9 m^5/N,
I_i = 2.8e6 kg/m^4, R_i = 1.4e8 N s/m^5, R_d = 1.4e7 N s/m^5

high damping needed to control engine resonances. The inertia track is modelled via a first order fluid system differential equation, where the fluid compliance term is neglected. Eq. (4) is non-linear as the R_i term depends on fluid variables:

$$I_i\dot{q}_i(t) + R_i(\Delta p_{12}, q_i)q_i(t) = p_2(t) - p_1(t) = \Delta p_{12}(t). \qquad (4)$$

The I_i term plays an important role but its measurement is very difficult [6].

Furthermore, an accurate estimate based on partial differential equations would require a complicated and lengthy analysis [10]. In an effort to characterize I_i, the flow through the inertia track can be assumed to be one-dimensional and steady flow. The inertia track is assumed to be a straight pipe of length l_i and area A_i. The inertance is $I_i = \rho l_i/A_i$ where ρ is the fluid density. Note that the effective length (l_i) could be between 1.0 and 1.33 of the geometric length [10].

The fluid resistance of a channel is the slope of the plot between pressure drop across a channel and the resulting flow rate through it. In general, the relation between steady state pressure drop
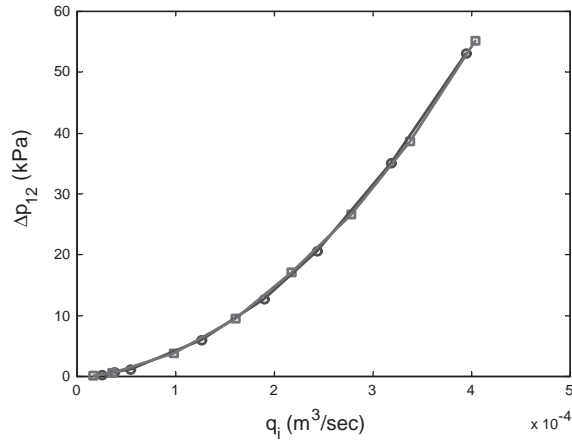
Fig. 5. Measured resistance characteristics of inertia track: O, water; □, anti-freeze mixture.

Table 2
Predicted and measured inertia track resistance R_i

Predicted	Capillary tube formula (Eqs. (2)–(6))	$R_i = 8.65e6 \text{ N s/m}^5$
	Sharp-edge orifice formula (Eqs. (2)–(7))	$R_i = 1.90e11 q_i \text{ N s/m}^5$
Measured	Linearization (at $q_i = 1e\text{-}4 \text{ m}^3/\text{s}$)	$R_i = 3.45e7 \text{ N s/m}^5$
	Second order poly-fit	$R_i = 3.45e11 q_i \text{ N s/m}^5$

(Δp_{12}) and steady flow rate (q_i) in a pipe is non-linear. Measured results of Fig. 5 verify this for the inertia track. The Δp_{12} is determined to be a function q_i^2 and the curves for water and anti-freeze mixture are identical. Assuming laminar flow in a capillary tube, the linearized resistance can be calculated using the following formula [10]: $R_i = 128\mu l_i/\pi d_i^4$ where μ, l_i and d_i denote the fluid viscosity, length, and hydraulic diameter. Table 2 shows that this formula underestimates the resistance. This is expected since it neglects the end effects and pressure losses due to cornering. The non-linear relationship between q_i and Δp_{12} is given by the sharp edge orifice formula as follows: $q_i = C_d A_i \sqrt{2\Delta p_{12}/\rho}$, where C_d is the coefficient of discharge. In our work, R_i is determined via a bench experiment [2]. Utilizing a centrifugal pump, steady state flow is generated, and circulated through the inertia track only. To avoid any leakage or bypass, the inertia track fixture is sealed using silicone and is clamped to the working table; the decoupler is blocked using epoxy. The volumetric flow rate q_i is measured using an electromagnetic flow meter, whereas the pressure difference Δp_{12} between the inlet and the outlet of the fixture is measured using a differential pressure transducer. Assuming turbulent flow for a sharp edge orifice, the ideal value of $C_d = 0.61$ can be used as a good approximation [10]. Fig. 5 shows measured Δp_{12} versus q_i curves that are used to find the results of Table 2. From Fig. 5 it can be seen that the plot is very close to a quadratic relationship. A quadratic curve fit for these measured results gives a fit of 99%. The non-linear formulation based on sharp-edge orifice formula matches with the curve fit plot with a coefficient with the same order of magnitude. However, the linearized coefficient from the curve fit and capillary tube differs by one order of magnitude (Table 2). So the second order (quadratic) curve fit is taken as the resistance equation.
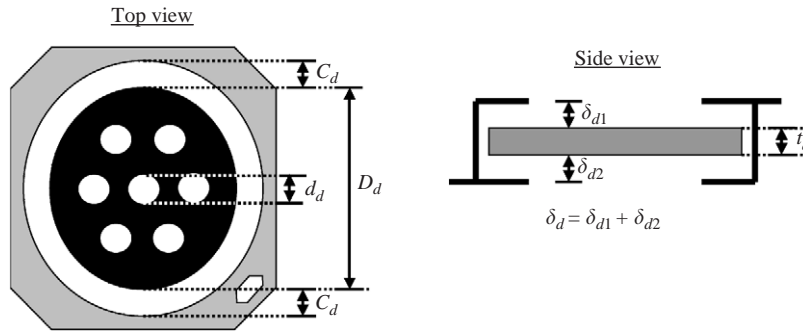
Fig. 6. Schematic of the decoupler.

2.3. Decoupler

As illustrated in Fig. 6, the decoupler contains a thin rubber disk of diameter D_d and thickness t_d. The disk freely moves between the top and bottom orifice plates where δ_d is the net decoupler gap. In our mount, seven small holes of diameter d_d expose the decoupler to the top and bottom chambers. To simplify our analysis, we eliminate the decoupler mechanism and allow the flow to take place only through the inertia track. To do this experimentally, the decoupler is fixed to the orifice plate using hard epoxy so that the flow through the decoupler q_d is blocked. The adhesive material must be sufficiently rigid so as not to introduce any additional compliance.

For the case of a free floating decoupler as shown in Fig. 6, the fluid flow is controlled by the decoupler switching mechanism, which couples or decouples the inertia track. When the disk floats in the middle of the gap, it will provide little fluid resistance R_d when compared with R_i. On the other hand, when the disk is at the top or at the bottom, q_d is zero, and thus the fluid can only flow through the inertia track. A linear model of the decoupler is given by a first order differential Eq. (5) where b_v and A_d denote the viscous damping coefficient and cross-sectional area of the decoupler gap. Further, m_d and x_d represent the disk mass and displacement of the decoupler:

$$m_d \ddot{x}_d(t) + b_v \dot{x}_d(t) = A_d[p_2(t) - p_1(t)]; \quad \dot{x}_d(t) = \frac{q_d(t)}{A_d}. \tag{5a–b}$$

Experimentally, the dynamics of decoupler is studied by installing a pressure transducer in the top chamber. The closing and opening events of the decoupler can be clearly observed in the top chamber pressure $p_1(t)$.

2.4. Elastomeric element

In a hydraulic mount, the role of the elastomeric element is mostly to support the static load, and to provide compliant chambers to contain the fluid. The rubber component is modelled using the Voigt's model, i.e., via linear spring (k_r) and damping (b_r) elements in parallel. Note that k_r and b_r can be determined with a dynamic characterization test on the MTS system when the fluid is drained out from the mount, and by removing the bottom chamber so as not have any air
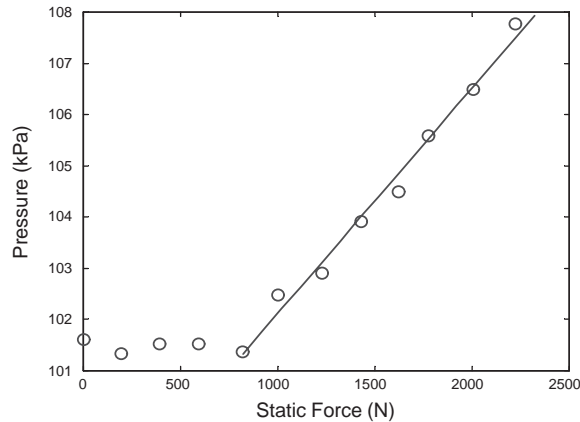
Fig. 7. Static top chamber pressure $\overline{p_1}$ corresponding to preload F_m: O, measured data; — , linear curve-fit.

entrainment effect. Compared to a typical hydraulic mount, the dynamic stiffness magnitude and phase values of the rubber element are low and virtually invariant at lower frequencies [5].

2.5. Chamber compliances

Linear fluid compliance is defined by $C = \Delta V/\Delta p$ where ΔV is the volume decrease and Δp is the pressure applied about an operating point. For a non-linear element, the p–V curve must be measured with a bench experiment [2], and the linearized compliance can be evaluated about an operating point. Unlike Kim and Singh [2], we estimate the compliance by placing the top chamber under a preload F_m. Such a load affects the mount in two ways. First, it affects the chamber pressure operating point ($\bar{p}$) about which the non-linear compliance is estimated. Depending on the severity of the non-linearity the location of the operating point will effect the dynamic stiffness. Second, it determines the mean fluid pressure p_m, which affects the behavior of entire fluid system. Kim [2] assumed that p_m is the same as the static pressure $\bar{p}$. In our study, we measured the static pressure as function of preload. Notice that since the bottom chamber is very compliant, the fluid pressure is virtually equal to the atmospheric pressure p_a when the preload is less than 1000 N, as shown in Fig. 7. The upper chamber pressure does not build up because the lower compliant chamber accommodates the fluid displaced very easily because of high compliance of lower chamber.

For the top chamber, the test is conducted under 0, 800 and 1200 N preloads. This static force was applied by the MTS system under manual static control [11]. The test results (Table 3) show that the C_1 value with 800 or 1200 N preload is much smaller than the one with zero preload. From simulations, it is seen that the dynamic stiffness predictions match measurements very well when C_1 is from 2e-11 to 3e-11 m^5/N. Therefore, a nominal value of $2.5\,m^5$/N is used for simulation. Fig. 8(b) shows that the bottom chamber compliance is quite non-linear and it exhibits some hysteresis due to loading and unloading. One may either linearize the curve about an operating point or curve fit it using a polynomial model, which in this case a third order fit is found to be sufficient. Also, note that p_2 typically stays almost constant due to a very compliant rubber diaphragm. Thus, the linearization yields a good approximation for C_2.

Table 3
Measured chamber compliance results

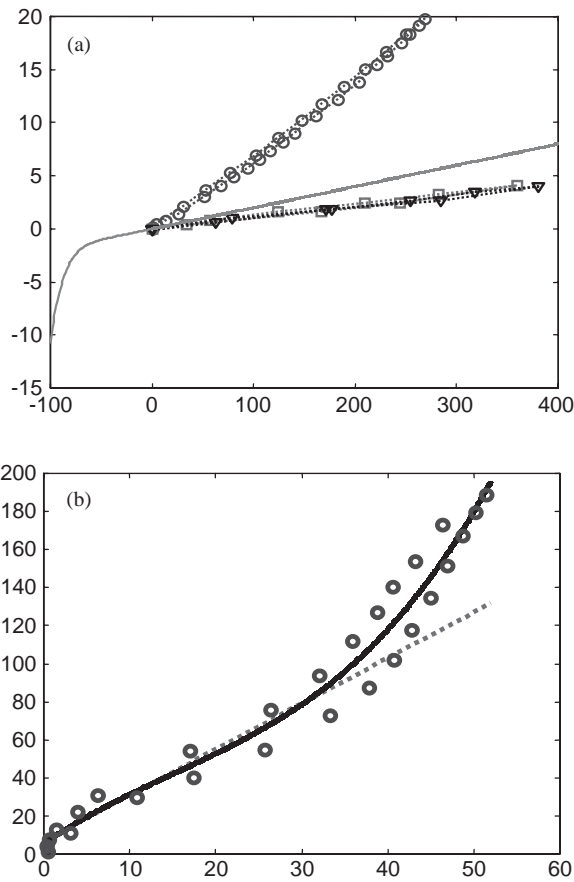| (a) Top chamber compliance		
Above p_a	$F_m = 0$ N	$C_1 = 7.29$e-11 m^5/N
	$F_m = -800$ N	$C_1 = 1.05$e-11 m^5/N
	$F_m = -1200$ N	$C_1 = 1.09$e-11 m^5/N
Below p_a	$C_1 = -7$e-45 $p_1^7 + 2.5$e-11	
(b) Bottom chamber compliance		
Linearization	$C_2 = 2.4$e-9 m^5/N	
Third order polynomial-fit	$C_2 = 1.51$e-18$p_2^3 - 6.82$e-14$p_2^2 + 3.13$e-9$p_2 + 5.19$e-6	

Fig. 8. p–V relationship for chambers: (a) top chamber: ·⊙·, preload = 0 N; ·□·, preload = 800 N; ·▽·, preload = 1200 N; —, preload used in simulation model; and (b) bottom chamber; ⊙, experimental curve; ▬, third order polynomial fit.

2.6. Vacuum phenomenon

A certain volume of gas can been assumed to be dissolved in the fluid but it comes out under reduced pressure. Kim and Singh [2] used the ideal gas law to determine a theoretical p–V
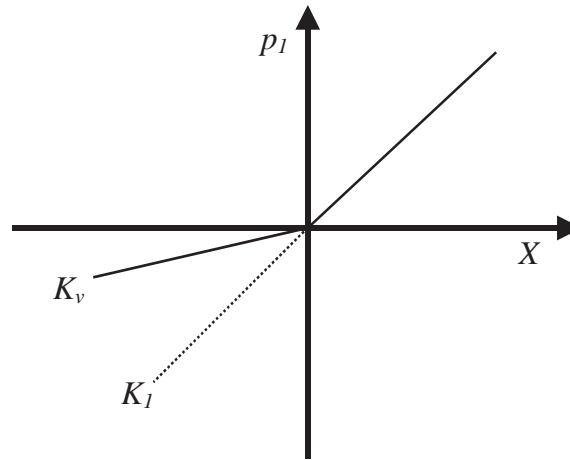
(a)
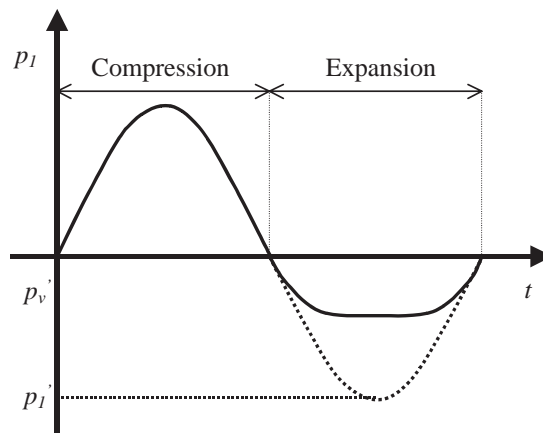
(b)

Fig. 9. Effect of vacuum on p_1: (a) asymmetric stiffness of top chamber; and (b) distortion in $p_1(t)$ waveform. —, with vacuum (K_v, p'_v); ···, without vacuum (K_1, p'_1).

relationship for the vacuum-like conditions. Since it is not easy to determine the amount of pre-dissolved gas, we propose to analyze the measured steady state dynamic results to determine the p–V relationship. Intuitively, it may be said that vacuum formation in the top chamber results in an increase in C_1. The net dynamic stiffness characteristics of the mount are then given by the corresponding stiffness K_1 under compression (when $p_1 > p_a$) and K_V for expansion (when $p_1 < p_a$) where p_a is the atmospheric pressure. The mount should thus behave as a non-linear system with a bi-linear stiffness curve as shown in Fig. 9(a). The corresponding pressure $p_1(t)$ should distort the pressure waveform below p_a. The level of distortion may be related to the relative strengths of K_1 and K_v as shown in Fig. 9(b). The stiffness K_1 for a compressive load has been estimated by a bench experiment and K_v is estimated based on the analysis of pressure waveform distortion.

Assume a piecewise linear system with stiffnesses K_1 and K_v as shown in Fig. 9(a). Consider the compressive compliance as unity since this is known from the bench experiment. Dynamic pressure amplitudes corresponding to vacuum and normal modes of operation, respectively, are

$$\frac{p_v'}{p_1'} = \frac{C_v}{C_1} = \frac{K_1}{K_v}. \tag{6}$$

From this relationship, the compliance under vacuum conditions C_v can be estimated. Such an analysis is done with the assumption that a change in stiffness from K_1 to K_v takes place in a discontinuous manner. In reality, the slope changes between the two states are less abrupt, and the transition takes place virtually instantaneously. This gradual change shows up in the measured p_1 waveform where no discontinuity is seen. In attempting to estimate C_v, one must also assume that the change in volume under the dynamic displacement excitation is the same as observed under static or quasi-static displacements. The resulting p–V relationship is given by the following empirical equation:

$$\frac{dV}{dp} = ap^n + b. \tag{7}$$

In our analysis, the polytropic coefficient n is found to range from 12 to 30. The coefficient a is about 10^{-60}, whereas b is the slope of the p–V curve given at the operating point $p_1 = p_a$. The small value of a in Eq. (7) points to a very sharp but continuous change in the stiffness (compliance) regime. These values were utilized for parametric studies, which finally yield a suitable value of n from 7 to 10 (Table 3). The governing p–V curves are then obtained for both chambers as shown in Fig. 8.

3. Linear lumped model

The governing equations developed in the last section can be linearized with certain assumptions [4]. For example, C_1 and C_2 are assumed to be constant over the range of operation, and only a linear R_i is considered. The decoupler (#d), as shown in Fig. 2, is modelled as a short length orifice, whose governing equation is the same as the inertia track (#i), as shown in Fig. 2, but with a lower resistance R_d and its inertance is ignored. The baseline parameters of the linear model are shown in Table 1. The governing equations are then defined as

$$q_i(t) + q_d(t) = A_p \dot{x}(t) - C_1 \dot{p}_1(t), \tag{8}$$

$$-q_i(t) - q_d(t) = C_2 \dot{p}_2(t), \tag{9}$$

$$F_T(t) = b_r \dot{x}(t) + k_r x(t) + A_p(\bar{p} - p_1(t)), \tag{10}$$

$$I_i \dot{q}_i(t) + R_i q_i(t) = p_2(t) - p_1(t), \tag{11}$$

$$R_d q_d(t) = p_2(t) - p_1(t). \tag{12}$$

Utilizing Eqs. (8)–(12), the dynamic stiffness (in Laplace domain s) can be defined by the following transfer function, whose coefficients are related to the linearized model parameters [4]. For a free decoupler mount, we obtain the third order in the numerator and the second order in

the denominator:

$$K_{32}(s) = \frac{F_T(s)}{x(s)} = \frac{\alpha_3 s^3 + \alpha_2 s^2 + \alpha_1 s + \alpha_0}{\beta_2 s^2 + \beta_1 s + \beta_0}, \tag{13a-f}$$

where

$$\alpha_3 = b_r C_1 C_2 R_d I_i, \quad \alpha_2 = C_1 C_2 R_d (b_r R_i + k_r I_i) + b_r I_i (C_1 + C_2) + A_r^2 C_2 R_d I_i,$$

$$\alpha_1 = b_r (R_i + Rd)(C_1 + C_2) + k_r C_1 C_2 R_d R_i + k_r I_i (C_1 + C_2) + A_r^2 I_i + A_r^2 C_2 R_d R_i,$$

$$\alpha_0 = k_r (R_d + R_i)(C_1 + C_2) + A_r^2 (R_d + R_i), \quad \beta_2 = C_1 C_2 R_d I_i,$$

$$\beta_1 = C_1 C_2 R_d R_i + I_i (C_1 + C_2), \quad \beta_0 = (R_d + R_i)(C_1 + C_2).$$

For a fixed decoupler mount, assuming $R_d \to \infty$, the coefficients of K_{32} reduce to

$$\alpha_3 = b_r C_1 C_2 I_i, \quad \alpha_2 = C_1 C_2 (b_r R_i + k_r I_i) + A_r^2 C_2 I_i,$$

$$\alpha_1 = b_r (C_1 + C_2) + k_r C_1 C_2 R_i + A_r^2 C_r R_i,$$

$$\alpha_0 = k_r (C_1 + C_2) + Ar^2, \quad \beta_2 = C_1 C_2 I_i,$$

$$\beta_1 = C_1 C_2 R_i, \quad \beta_0 = C_1 + C_2. \tag{13g-h}$$

Assuming $b_r = 0$ [5] and $C_2 \gg C_1$, K_{32} can be simplified to a second/second order transfer function for a free decoupler as suggested by Singh et al. [4] where γ is the static stiffness:

$$K_{22}(s) = \gamma \frac{\hat{\alpha}_2 s^2 + \hat{\alpha}_1 s + 1}{\hat{\beta}_2 s^2 + \hat{\beta}_1 s + 1}, \tag{14a}$$

where

$$\gamma = k_r + \left(\frac{A_r^2}{C_1 + C_2}\right), \quad \hat{\alpha}_2 = \left(\frac{R_d}{R_d + R_i}\right)\left(\frac{A_r^2}{k_r} + C_1\right) I_i,$$

$$\hat{\alpha}_1 = \left(\frac{1}{R_d + R_i}\right)\left(I_i + R_d R_i\left(\frac{A_r^2}{k_r} + C_1\right)\right), \quad \hat{\beta}_2 = \left(\frac{1}{R_d + R_i}\right)(I_i R_d C_1),$$

$$\hat{\beta}_1 = \left(\frac{1}{R_d + R_i}\right)(R_d R_i C_1 + I_i). \tag{14b-f}$$

Similarly, for the fixed decoupler case, the coefficients of K_{22} are reduced to the following, again as suggested by Singh et al. [4]:

$$\gamma = k_r + \left(\frac{A_r^2}{C_1 + C_2}\right), \quad \hat{\alpha}_2 = I_i\left(\frac{A_r^2}{k_r} + C_1\right),$$

$$\hat{\alpha}_1 = R_i\left(\frac{A_r^2}{k_r} + C_1\right), \quad \hat{\beta}_2 = I_i C_1, \quad \hat{\beta}_1 = R_i C_1. \tag{4g-j}$$

4. Non-linear model

4.1. Formulation

Based on the lumped parameter model of Section 2, a non-linear simulation model in the Matlab/ Simulink environment [12] is developed. Except for the decoupler, non-linear components can be modelled via continuous non-linear functions. Such continuous relationships are obtained either experimentally or via mathematical descriptions of the physical processes. Some non-linearities can be linearized provided the dynamic excursion range is small. This holds true for $p_2(t)$ because C_2 is very high and the associated dynamic excursions are close to the atmospheric pressure. Also, the top pressure chamber exhibits an asymmetric non-linearity, but the stiffness in both regimes is treated as linear with very different slopes and the transition at $p_1 = p_a$ is assumed to be continuous. In some cases, the polynomial curve-fit is employed. The non-linear model is solved employing the fourth order Runge–Kutta method with a fixed time step [12]. The total time to run the steady state simulation model for a particular X and f of excitation is specified by $60T$, where $T = 1/f$ is the period of excitation. Of the $60T$ time span, the first $40T$ is used to overcome the starting transient effects due to the numerical integration of non-linear equation. Data from the rest of the time ($20T$) is used for time or frequency domain validation process. The free decoupler model consumes more time due to the additional nonlinearity introduced by the decoupler mechanism.

4.2. Fixed decoupler model

A comparison of experimental results [13] between the fixed and free decoupler cases shows that the non-linearity is caused mostly by the vacuum pressure created in the top chamber and the decoupler switching action. The distortion of the sinusoidal pressure waveform because of vacuum is dominant for both the fixed and free decoupler case. The elimination of decoupler focuses the study on the formation of vacuum, which is still poorly understood. The initial conditions for $p_1(t)$ and $p_2(t)$ are set as atmospheric pressure p_a. Since the compliance of each chamber is non-linear, at each time step, the operating pressure is used to estimate C_1 and C_2 from the measured p–V curves. Each compliance (C_1 or C_2) is expressed as a polynomial function of pressure (p_1 or p_2), as shown in Table 2. The dynamic pressures $p_1(t)$ and $p_2(t)$ calculated throughout the simulation are gage pressures (above or below p_a).

The simulink model of the inertia track sub-system is constructed based on Eq. (4). The Δp_{12} due to R_i element is utilized as a feedback loop to this system. The non-linear resistance R_i is specified as a function of q_i, as shown in Table 2. The initial condition for q_i is zero since the simulation is assumed to start from the static equilibrium condition. The transmitted force sub-system calculates the components contributed by both rubber and fluid elements, as shown by Eq. (3). The rubber stiffness k_r and damping b_r are interpolated from measured data by employing a look-up table, while p_1 is calculated numerically from the top chamber sub-system.

4.3. Free decoupler model

In the free decoupler model, yet another sub-system associated with a free floating disk (Fig. 6) is integrated in the mount model. The equation of motion for the decoupler gap is based on the

equations derived for the dashpot model Eqs. (5a–b). The decoupler sub-system has to be enabled or disabled depending whether the decoupler opens or closes. The states of the system such as $\dot{x}_d$ and x_d have to be held or reset to zero whenever the decoupler closes. The initial condition for the decoupler variable x_d is set as δ_d (Fig. 6), depending on whether the disk has lower or higher density then the surrounding fluid, which makes the decoupler 'float' ($x_d = \delta_d$) or 'sink' ($x_d = 0$). The decoupler sub-system calculates the flow rate through the decoupler q_d based on disk velocity $\dot{x}_d$, as shown in Eq. (5b). When the decoupler closes, we assume that the flow takes place only through the inertia track since the decoupler mechanism is designed so that $q_d = 0$, although small amount of leakage may occur [9]. Such enable/disable signals control the decoupler switching mechanism, thereby introducing the discontinuous non-linear characteristics in our model.

4.4. Comparison of alternate decoupler models

Three alternate approaches to model the decoupler mechanism have been previously employed. First, Kim and Singh [5] utilize a kinematic switching analysis to predict the time events corresponding to the decoupler opening and closing. This is done by calculating the fluid volume transferred through the decoupler between the top and bottom chambers and compare them with the regimes where the decoupler can freely float. Employing this method, a complicated analysis of the decoupler motion can be avoided, while still achieving a good approximation. Second, Colgate et al. [6] claimed that a squeeze film between the decoupler disk and orifice plates produces a damping force against the disk movement. The squeeze film force is inversely proportional to the cube of the decoupler gap. Linearization of the damping force was performed by considering only the fundamental harmonics of its Fourier contents and neglecting higher order harmonics. Third, Royston and Singh [14] modelled the compliance in the decoupler orifice plate or the mechanical stops as a cubic (continuous) spring. The polynomial (continuous) stiffness expression was chosen since it could be more easily handled than a piecewise linear (clearance) model.

4.5. Decoupler switching mechanism

The decoupler is designed so that the mount can provide different operating conditions for small or large excitation. In the small amplitude case, the decoupler of our example case is wide open most of the time, while in the large amplitude response, the decoupler is partially open. When the decoupler is open, $q = q_i + q_d$, but when it is closed, $q = q_i$. Fig. 10 shows the typical response corresponding to a large amplitude excitation; refer to Fig. 3 for the sign convention. To better understand the phenomenon, the sequence of events is divided into five steps.

Step 1: For the given mount the decoupler floats. So, the disk is assumed to be at the top ($x_d = \delta_d$) and the gap is closed, and hence $q_d = 0$ and $q = q_i$.

Step 2: When $p_1 > p_2$, the decoupler starts to move down (open) and as a result, the fluid flow through the decoupler q_d tries to equalize the p_1 and p_2, and oppose an increase in p_1. Notice that q_i is still > 0 although the disk is moving downward. This is due to the inertance effect of the inertia track.

Step 3: The disk is at the bottom ($x_d = 0$) and the decoupler gap is closed ($q_d = 0$). Due to the decreasing q_i, p_1 increases. Then q_i changes direction, which causes p_1 to decrease.
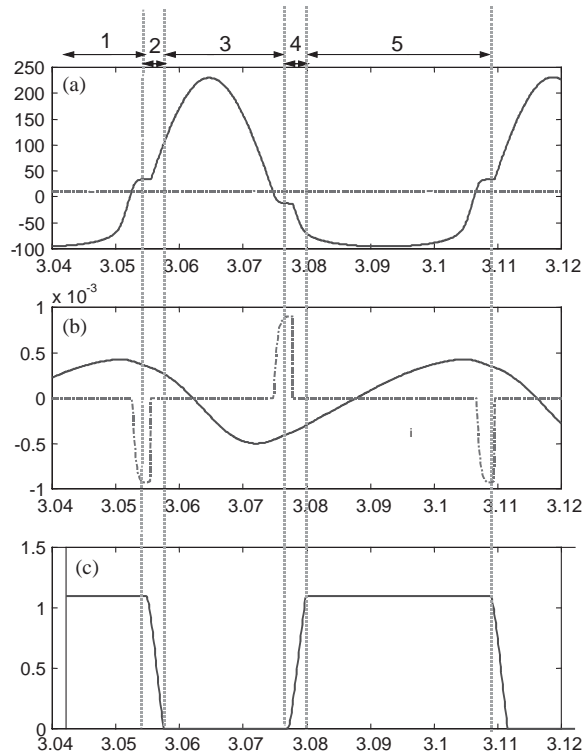
Fig. 10. Typical decoupler switching stages corresponding to a sinusoidal displacement excitation of large amplitude ($X = 0.75$ mm, $f = 18.5$ Hz): (a) ——, p_1, upper chamber pressure; $-\cdot-\cdot-\cdot$, p_2, lower chamber pressure; (b) ——, q_i, flow through inertia track; $-\cdot-\cdot-\cdot$, q_d, flow rate through decoupler; and (c) decoupler displacement.

Step 4: When $p_1 < p_2$, the disk starts to move up (gap is now open), and the p_1 suddenly stops varying until the decoupler is closed again.

Step 5: The decoupler disk is at the top, and as $x(t)$ and q_i move upward. Vacuum is now generated. During this stage, $p_1 < p_2$ and $p_1 < p_a$. When $x(t)$ changes direction, p_1 again starts to increase.

Steps 2–5 continue to repeat themselves. The decoupler equation of motion is then described as

$$\ddot{x}_d(t) = \begin{cases} \dfrac{A_d[p_2(t) - p_1(t)]}{m_d} - \dfrac{b_v \dot{x}_d(t)}{m_d} & \text{for } 0 < x_d(t) < \delta_d, \\ 0, \dot{x}_d(t) = 0 & \text{when } x_d(t) = 0 \text{ and } x_d(t) = \delta_d. \end{cases} \tag{15}$$

In measured results, high frequency fluctuations are observed at those times when the decoupler is open (steps 2 and 4). Some of these phenomenons are also captured by our simulation even at low excitation frequency.

4.6. Decoupler damping model

The damping associated with decoupler is difficult to estimate experimentally as it would require the measurement of transient flow. Steady state experimental results (based on loss angle

spectra) do, however, show high damping in the decoupler. Colgate et al. [6] suggested that the squeeze film damping force F_s opposes the decoupler when it is about to close. Assuming that there is no opening in the decoupler plate, F_s is defined as [15]

$$F_s = b_s \dot{x}_d, \quad b_s = \frac{3\mu r_d}{2\Delta^3}, \qquad (16a-b)$$

where μ, r_d, and Δ denote, respectively, the viscosity of water, decoupler radius, and the remaining gap between decoupler and top (or bottom) orifice plate as the disk is about to close at the top (or bottom). For our case, $\Delta = \delta_d - x_d$ when $\dot{x}_d > 0$, and $\Delta = x_d$ when $\dot{x}_d < 0$. Note that since F_s is inversely proportional to Δ^3, the squeeze film force will therefore increase very rapidly as the decoupler is bottoming out. Assuming a linear velocity profile, steady flow, and constant μ, the viscous damping force F_v due to the shear stresses acting on the side of the decoupler can be defined as [16]

$$F_v = b_v \dot{x}_d, \quad b_v = \frac{\mu A_v}{c}, \qquad (17)$$

where c is the clearance gap between decoupler and orifice plate, and A_v is the viscous force area. Fig. 11 compares the squeeze film and viscous damping coefficients as a function of the remaining decoupler gap Δ. Observe that b_v is very small, of the order of 10^{-2} N s/m, while b_s ranges from ∞ to $10°$ N s/m. The damping introduced in the decoupler system is from the oscillatory motion of the decoupler inside the cage. The mechanism for damping appears to be a combination of squeeze film and viscous damping elements. Sample calculations, as shown in Fig. 11, yield vastly
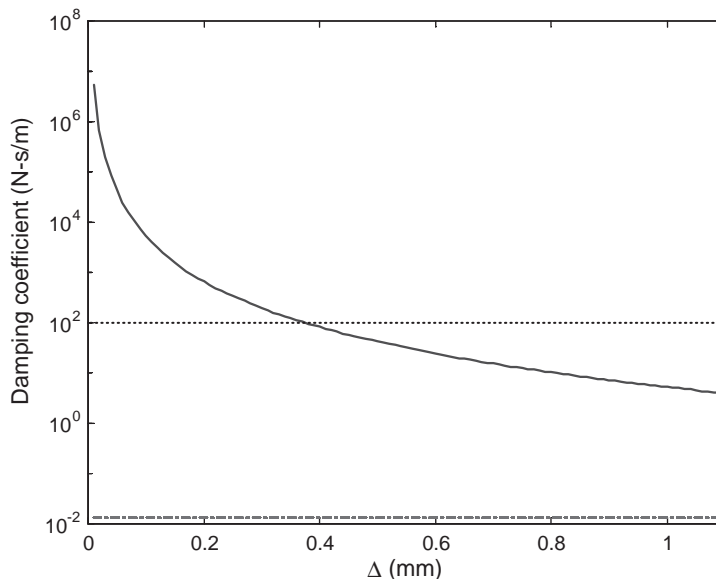

Fig. 11. Comparison of squeeze film and viscous damping coefficient for a free decoupler: —, b_s; - · - ·, b_v; · · ·, b_{ve}.

different values of b_s and b_v. Therefore, we define an equivalent viscous damping coefficient $b_{ve} = 100$ N s/m based on parametric studies. This model worked extremely well without creating any numerical problems introduced by the squeeze film formulation, especially when Δ is very small.

5. Experimental methodology

5.1. Bench experiments

Bench experiments are constructed to study the non-linear characteristics of C_1, C_2, and R_i. The objectives of these experiments is to determine whether the non-linear characteristics can be modeled by simplified theoretical expressions. Alternatively, empirical results must be incorporated in simulation. Refs. [2,13] discuss these in more detail.

5.2. Steady state experiments

Sinusoidal dynamic tests have been done using the MTS (model 831.50, 1000 Hz) elastomer test system [11]. Two configurations of the take-apart mount are used for study: (a) free decoupler mount (with both decoupler and inertia track) and (b) fixed decoupler mount (without any decoupler). The take-apart mount is assembled in a water bath so as not to include any air. The assembly is done with a clamping fixture. Care has to be taken that there are no bubbles in the water bath, which can be trapped during the assembly of the mount. For maintaining a low level of dissolved air, the water temperature should be kept low.

The internal dynamics is studied by installing a pressure transducer in the top chamber and measuring the dynamic $p_1(t)$. This can accurately map the dynamic stages of the decoupler as the $p_1(t)$ waveform gives a very good understanding of the internal dynamics. Two kinds of pressure transducer were used for experimentation: (a) absolute pressure transducer (strain gage), and (b) dynamic pressure transducer (piezoelectric). The absolute pressure transducer is primarily used for recording the mean $\bar{p}_1$ level, while the dynamic pressure transducer is used for accurately recording $p_1(t)$. Under the static manual control of the MTS controller, the mount was subjected to varying loads and $\bar{p}_1$ was recorded. This gave an estimate of the initial pressure to be used for simulation. Dynamic characterization experiments were conducted at $X = 0.15$, 0.25, 0.5, 0.75, 1.0, 1.25, and 1.5 mm over 2.5–50 Hz. Both frequency and time domain results were analyzed for two mount configurations (with and without decoupler). Theoretical results match well with experimental results (Fig. 12). Time domain results from the fixed decoupler (only inertia track) case permit an examination of vacuum formation under certain conditions of excitation amplitude and frequency.

5.3. Transient response experiments

A transient displacement input $x(t)$ was applied to the mount using the MTS system. The servohydraulic system was programmed in the displacement control mode for applying a single 'rectangular' (step up and step down), triangular and sawtooth waveforms. All such
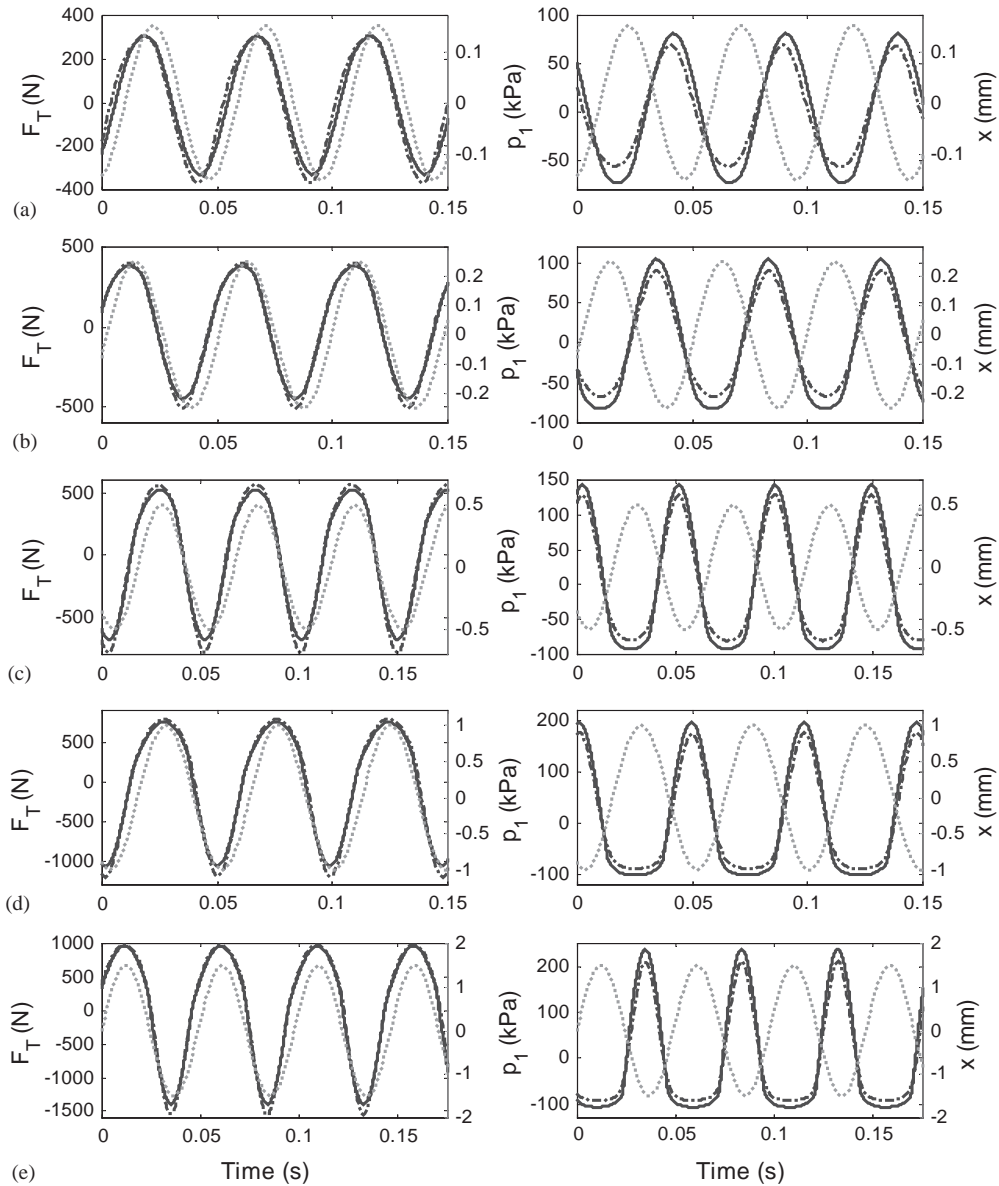
Fig. 12. Predicted and measured steady state time domain responses of the fixed decoupler mount for the case of $f = 20.5$ Hz: —, simulation (F_T and p_1); -·-·, measured (F_T and p_1); ···, x. (a) $X = 0.15$ mm; (b) $X = 0.25$ mm; (c) $X = 0.5$ mm; (d) $X = 1.0$ mm; and (e) $X = 1.5$ mm.

excitations were applied over a mean displacement input x_m corresponding to an F_m of about 1200 N. The top chamber pressure $p_1(t)$, transmitted force $F_t(t)$, and displacement excitation $x(t)$ signals were acquired and processed using the digital system that is independent of the MTS machine.
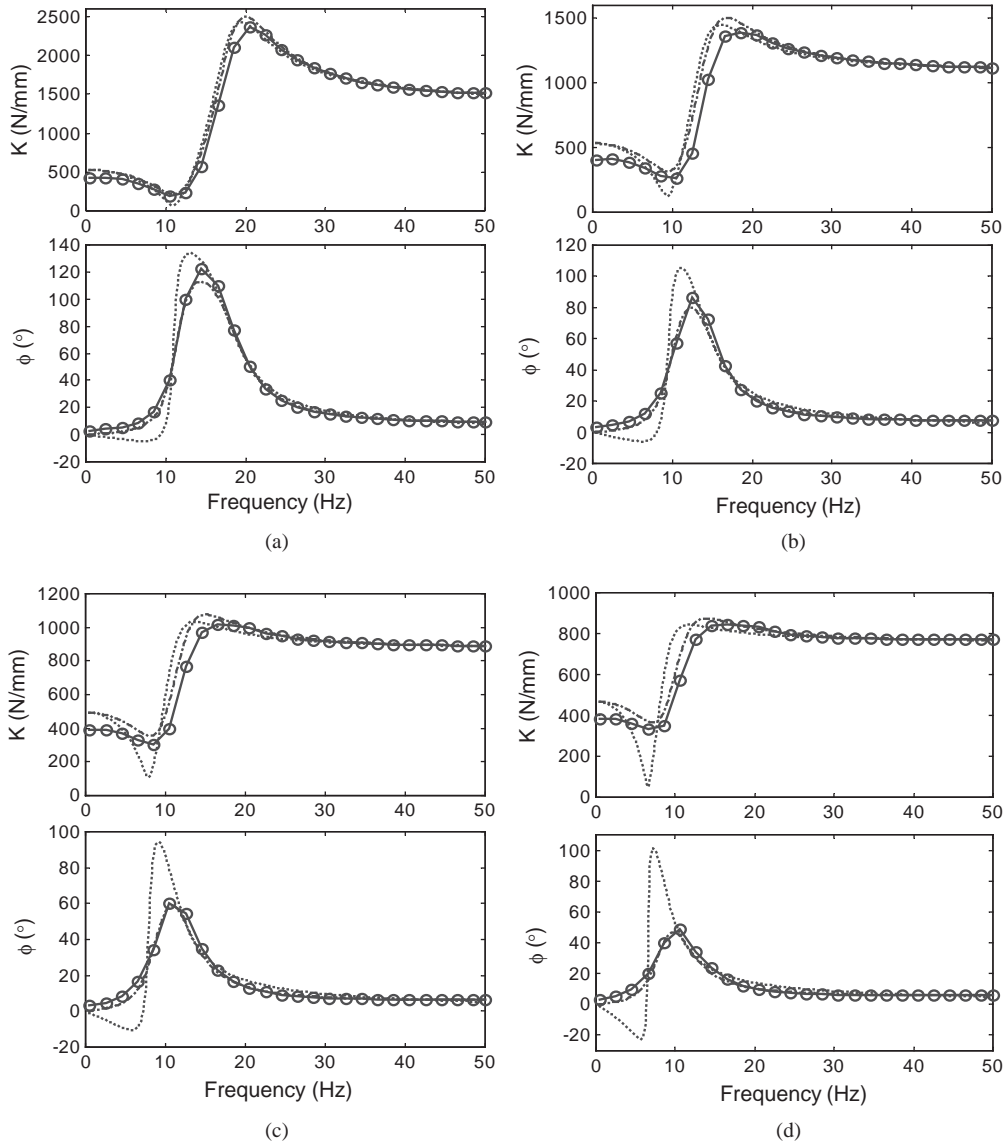
Fig. 13. Dynamic stiffness spectra of fixed decoupler mount: –⊖– measured; -·-·-, K_{32} curve-fit; ···, K_{22} curve-fit. (a) $X = 0.15$ mm; (b) $X = 0.5$ mm; (c) $X = 1.0$ mm; and (d) $X = 1.5$ mm.

6. Results of linear model

6.1. Transfer function curve-fits

Measured dynamic stiffness data for both fixed ($R_d \rightarrow \infty$) and free (finite R_d) decoupler mounts are curve fitted, and compared with theory of Section 3. For the case of the fixed decoupler mount, Fig. 13 shows that the $K_{32}(s)$ model (Eq. (13)) fits the measured stiffness magnitude K and
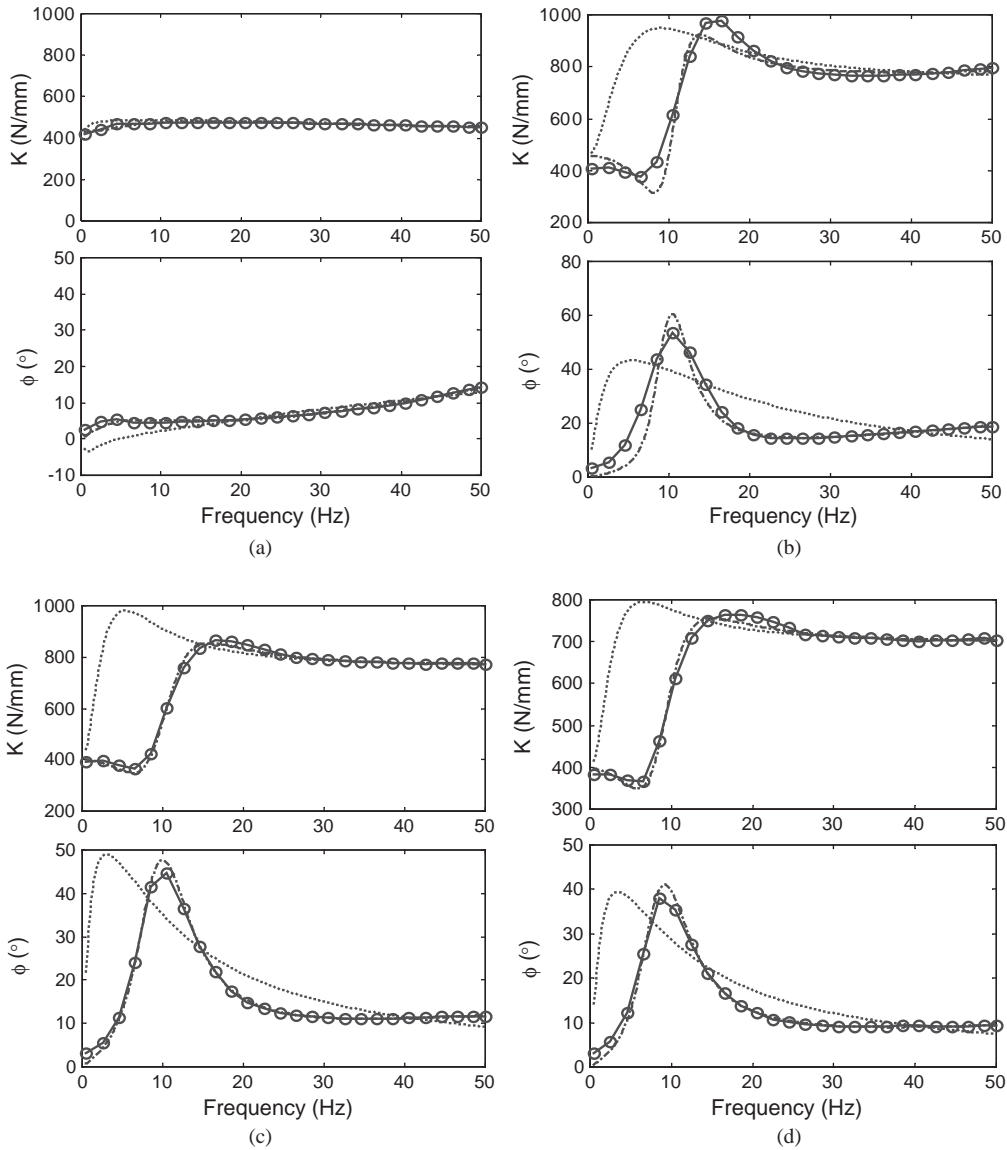
Fig. 14. Dynamic stiffness spectra of free decoupler mount: –⊖– measured; - - - -, K_{32} curve-fit; ⋯, K_{22} curve-fit. (a) $X = 0.15$ mm; (b) $X = 0.5$ mm; (c) $X = 1.0$ mm; and (d) $X = 1.5$ mm.

phase ϕ spectra very well. Conversely, the $K_{22}(s)$ model (Eq. (14)) predicts K very well, but not ϕ, especially at large X. For the free decoupler mount (Fig. 14), the $K_{22}(s)$ model can only predict the small amplitude response ($X = 0.15$ mm), but an excellent match is obtained with the $K_{32}(s)$ model. At higher X (0.5, 1.0, and 1.5 mm), frequencies that yield maximum K and ϕ maximum are predicted to be much lower with the $K_{22}(s)$ model than those observed in measured results. Overall, we can see that the $K_{32}(s)$ model gives better curve fits and is able to predict measured data for different X and f. However, the $K_{22}(s)$ model is reasonable at certain X values.
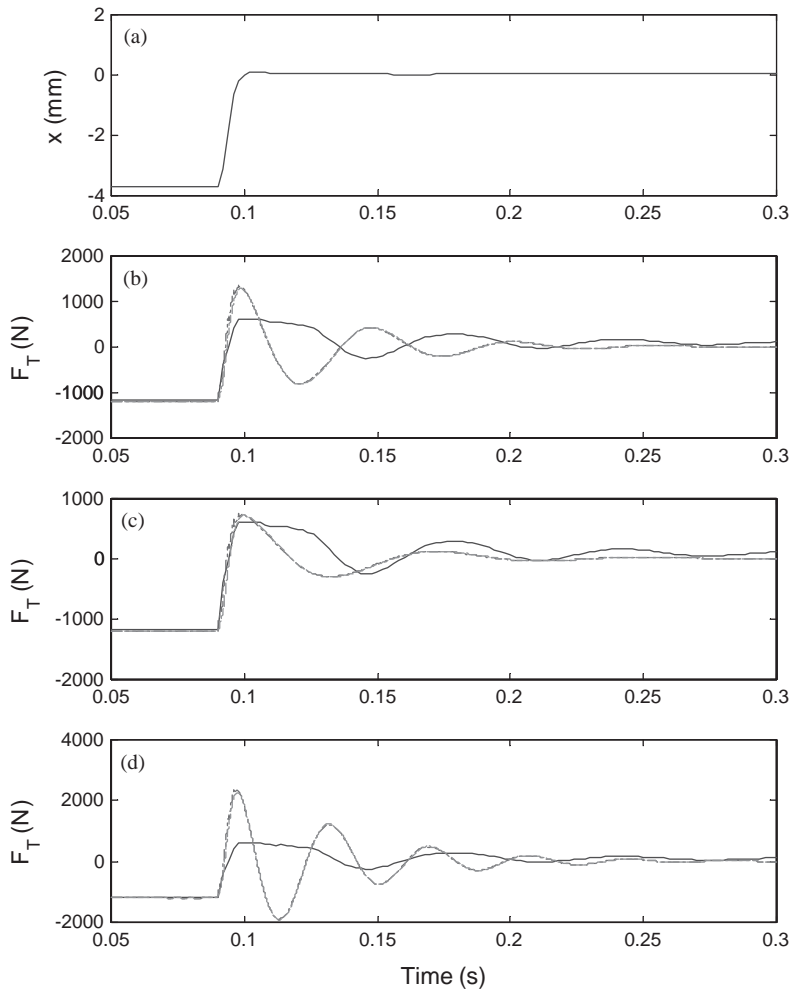
Fig. 15. Step response of fixed decoupler mount given effective C_{1e}: —, measured; - - -, K_{32} curve-fit model; $\cdots$, K_{22} order curve-fit model: (a) Displacement excitation amplitude; (b) model with compliance value same as upper chamber compliance; (c) model with compliance value twice that of upper chamber compliance; and (d) model with compliance value half of upper chamber compliance.

6.2. Transient response

Although the transfer function models of Section 3 are constructed for frequency domain analysis purposes, it is interesting to observe the time domain response. Step and pulse responses of the $K_{32}(s)$ and $K_{22}(s)$ models (Eqs. (13) and (14)) are compared with measured results. Although the linear model assumes that C_1 is constant, this assumption is not valid as the formation of vacuum induces an asymmetric stiffness characteristic. Therefore, a parametric study is conducted to evaluate the effects of C_1 on the transient response. Comparisons between simulation and experiment are based on the overshoot, settling time, and natural frequency of the transmitted force oscillations.
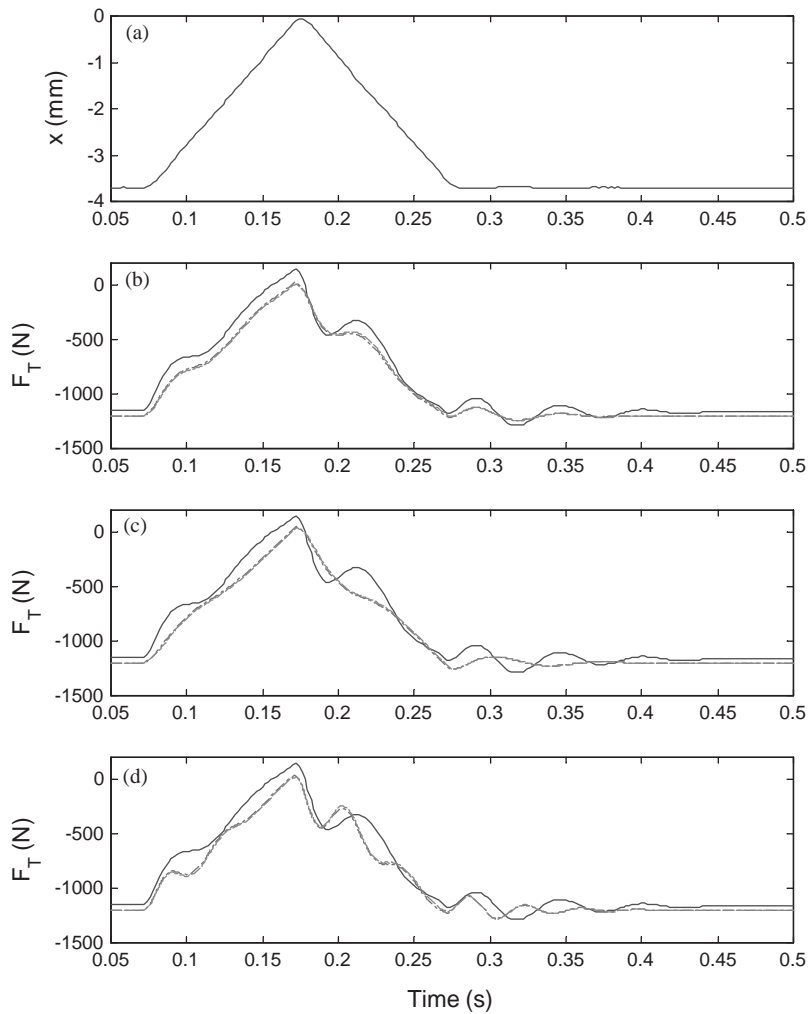
Fig. 16. Pulse response of fixed decoupler mount given effective C_{1e}: —, measured; -·-·, K_{32} curve-fit model; ···, K_{22} order curve-fit model. (a) Displacement excitation amplitude; (b) model with compliance value same as upper chamber compliance; (c) model with compliance value twice that of upper chamber compliance; and (d) model with compliance value half of upper chamber compliance.

The step response of Fig. 15 shows that the linear model matches best when the effective $C_{1e} = 2.0\,C_1$, where C_1 is the baseline nominal value. But the pulse response of Fig. 16 works well when $C_{1e} = C_1$. In the step response, C_{1e} is larger than C_1 since a lot of vacuum is generated due to high amplitude of excitation and a short transient duration of $x(t)$. Conversely, in the pulse response, C_{1e} is about the same as C_1 since $x(t)$ is not as suddenly applied as the step input, resulting in less vacuum generated. The effect of vacuum is also seen in the measured F_T profile; observe flat regime around the first overshoot. Fig. 17 shows that p_1 is very low during this regime. Therefore, in this case, the generation of vacuum adds some damping to the system, especially to the first peak. For a pulse response, the formation of vacuum is less as can be seen from the lesser
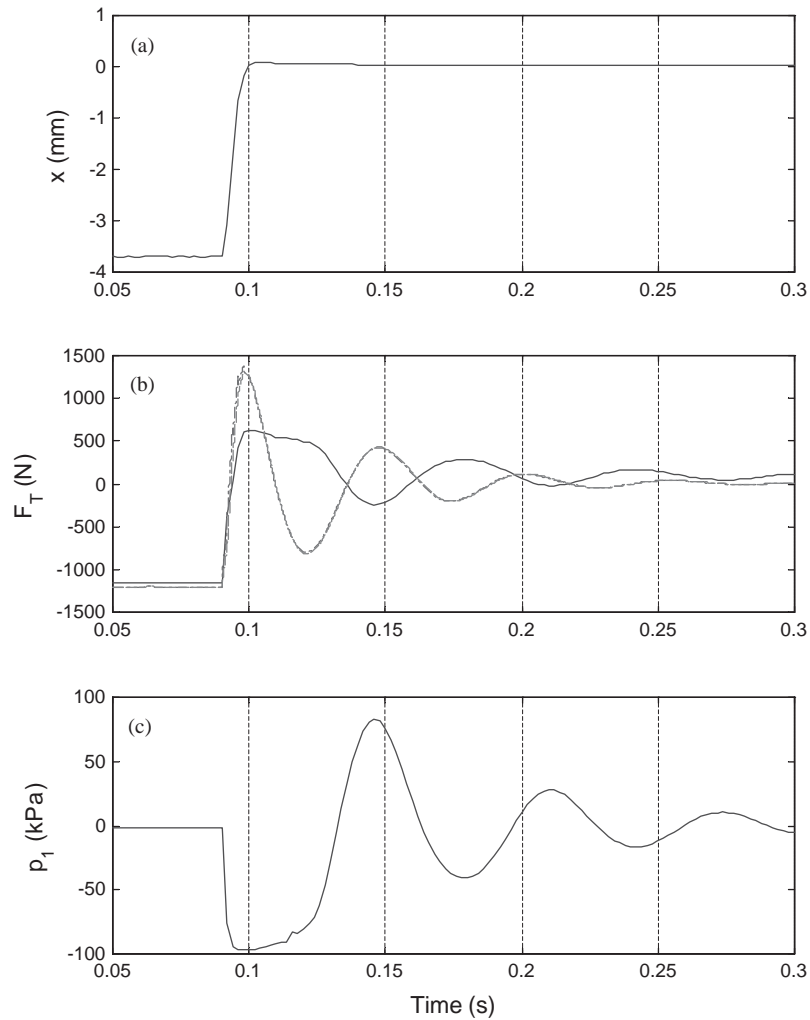
Fig. 17. Effect of vacuum on the top chamber pressure and transmitted force given step displacement input to a fixed decoupler mount: —, measured; -·-·, K_{32} curve-fit model; ···, K_{22} order curve-fit model. (a) Displacement excitation profile; (b) transmitted force; and (c) upper chamber pressure.

deformation of the p_1 waveform as shown in Fig. 18. This is again due to a gradual increase in the loading. In both step and pulse responses, $K_{22}(s)$ and $K_{32}(s)$ models predict almost the same results.

7. Transient response using non-linear model

Although the frequency domain formulations seem to match very well with measurements, a more important and yet difficult task in the model validation process is to compare the time domain responses. In such cases, the non-linearities due to the vacuum and the decoupler
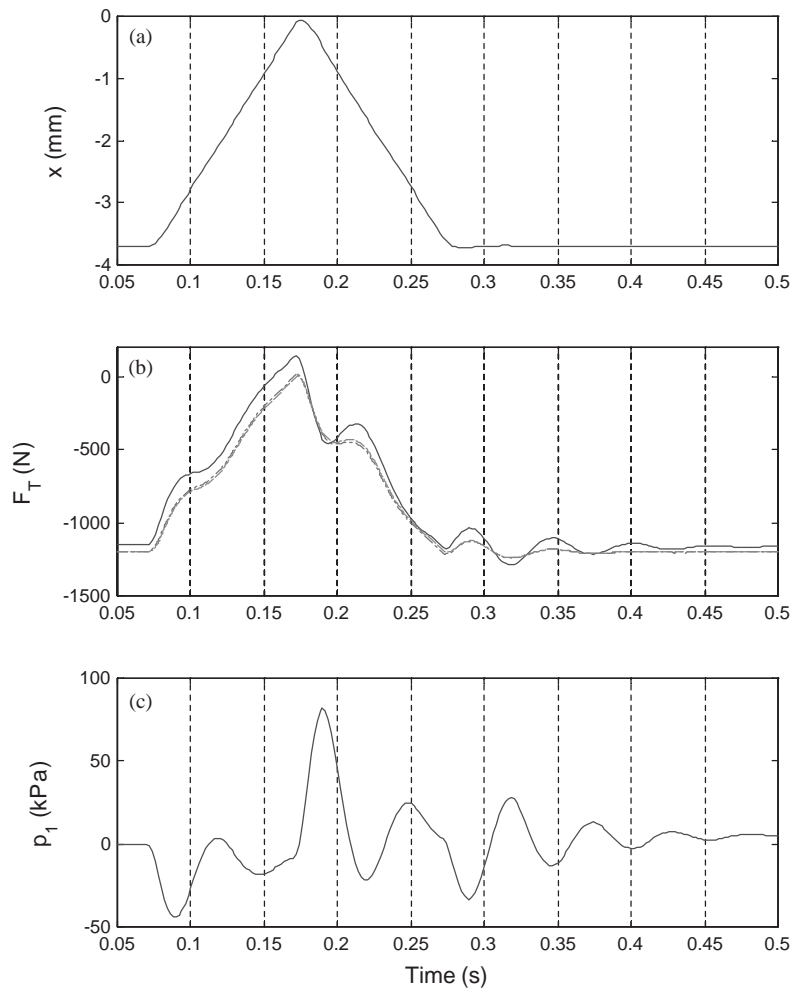
Fig. 18. Effect of vacuum on the top chamber pressure and transmitted force given pulse displacement input to a fixed decoupler mount: —, measured; $-\cdots-$, K_{32} curve-fit model; $\cdots$, K_{22} order curve-fit model. (a) Displacement excitation profile; (b) transmitted force; and (c) upper chamber pressure.

mechanism can be clearly seen. Transient response simulations are conducted by applying step and pulse displacement inputs corresponding to the experimental waveforms. For example, Fig. 19 shows the measured waveforms corresponding to step up and down transients. The step-up displacement of Fig. 20 or Fig. 22 is obtained by applying a 1200 N (say B) compressive preload, and then releasing it to 0 N (say A); the procedure is reversed for step-down. The pulse input is acquired by applying a preload $B = 1200$ N, releasing to $A = 0$ N in 0.1 s and compressing it again to B in yet another 0.1 s.

For the step input (Figs. 20 and 22), measured F_T and p_1 show a faster decay than predicted results. This might be caused by the unmodelled dynamics associated with the inertia track. The period of the decaying oscillations is smaller for the simulation. This might due to the amplitude and frequency dependence of C_1. The vacuum formation reduces the expected overshoot for both
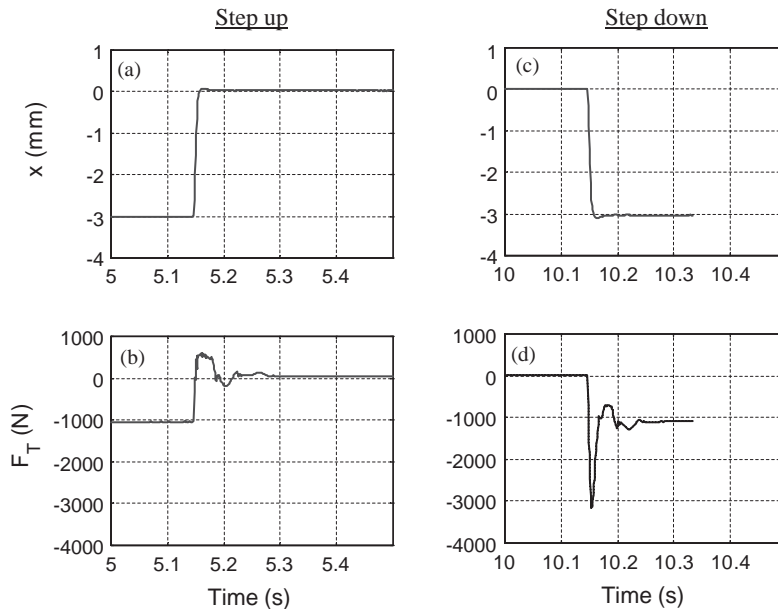
Fig. 19. Measured step up and step down displacement excitation and transmitted force waveforms for a free decoupler mount: (a) Step up displacement excitation profile; (b) transmitted force for step up excitation; (c) step down displacement excitation profile; and (d) transmitted force for step down excitation.

simulation and experiment. An impulse input to the mount is difficult to experimentally achieve and therefore a triangular waveform is used. There is a limit to the pulse width that can be achieved by a servo-hydraulic test system. Further, a reduction in the pulse time makes it difficult to achieve the peak amplitude. The triangular excitation subjects the mount to a gradual ramp input (Figs. 21 and 23). The transmitted force $F_T(t)$ and top chamber pressure $p_1(t)$ from simulation and experiment match very well although predictions show less damping and a slower decay of oscillations. The forces transmitted by the mount for step up and step down displacements are different. The $F_T(t)$ peak during the step up (B to A) is less than the force transmitted during the step down (A to B) as shown in Fig. 19. This further strengthens our claim that the mount behaves in an asymmetric manner. The role of vacuum formation is very dominant in controlling such an asymmetric behavior.

For the free decoupler case, q_i, q_d, and x_d time histories are plotted for a better understanding of the inertia track dynamics and the decoupler switching mechanism. Fig. 22 shows that when compared to the case of fixed decoupler (Fig. 20), the addition of a free decoupler results in reduced oscillations. This suggests that the decoupler introduces damping to the system. Decoupler action comes out very prominently in the simulated waveforms (Figs. 22 and 23) of p_1 and F_T. As the decoupler closes, p_1 rises significantly as shown by the small 'bumps'. The disk displacement x_d is also plotted to illustrate the sequencing mechanism. One final note regarding the measured $p_1(t)$ histories is that p_1 is measured using a dynamic transducer with a lower frequency limit of 0.5 Hz. Consequently, measured results show a very low frequency trend or drift. Such trends are not obviously seen in simulations.
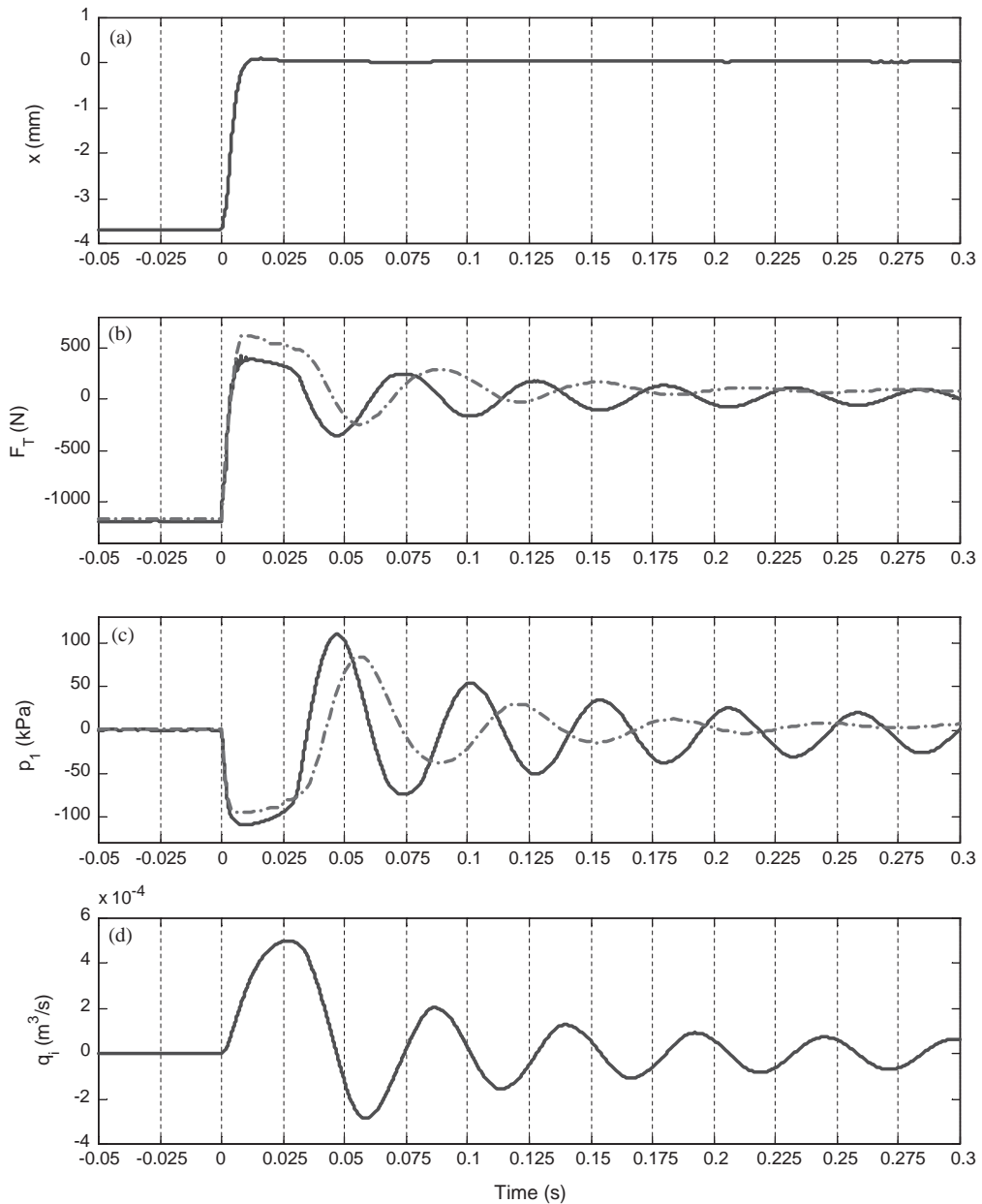
Fig. 20. Step response of the fixed decoupler mount. Key for F_T and p_1 plots: —, simulation; -·-·, measured; (a) displacement excitation profile; (b) transmitted force; (c) upper chamber pressure; and (d) flow through inertia track.

8. Conclusion

Chief contribution of this article has been to develop a model that can predict mount response to transient events experienced by an automotive engine. The step up or down and the pulse transients
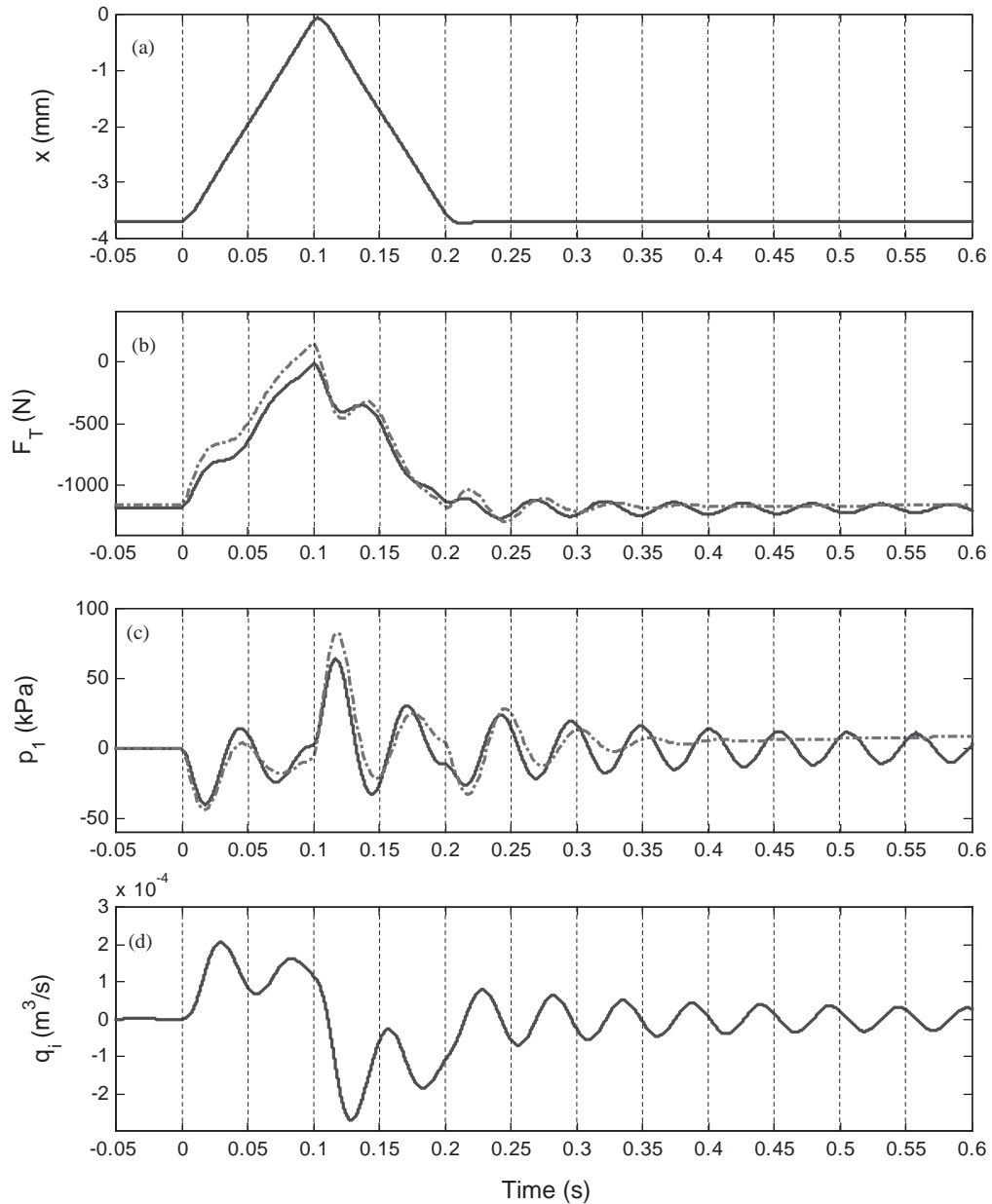
Fig. 21. Pulse response of the fixed decoupler mount. Key for F_T and p_1 plots: —, simulation; -·-·, measured; (a) displacement excitation profile; (b) transmitted force; (c) upper chamber pressure; and (d) flow through inertia track.

analyzed in this study represent typical loading profiles. This paper has successfully simulated such conditions for the first time in terms of both experimental and analytical studies. Our analysis is however limited to the lower frequencies ($\leqslant 50\,\mathrm{Hz}$) and accordingly several assumptions have been made [4,10]. For instance, the damping of elastomeric element can be assumed to be negligible [5].
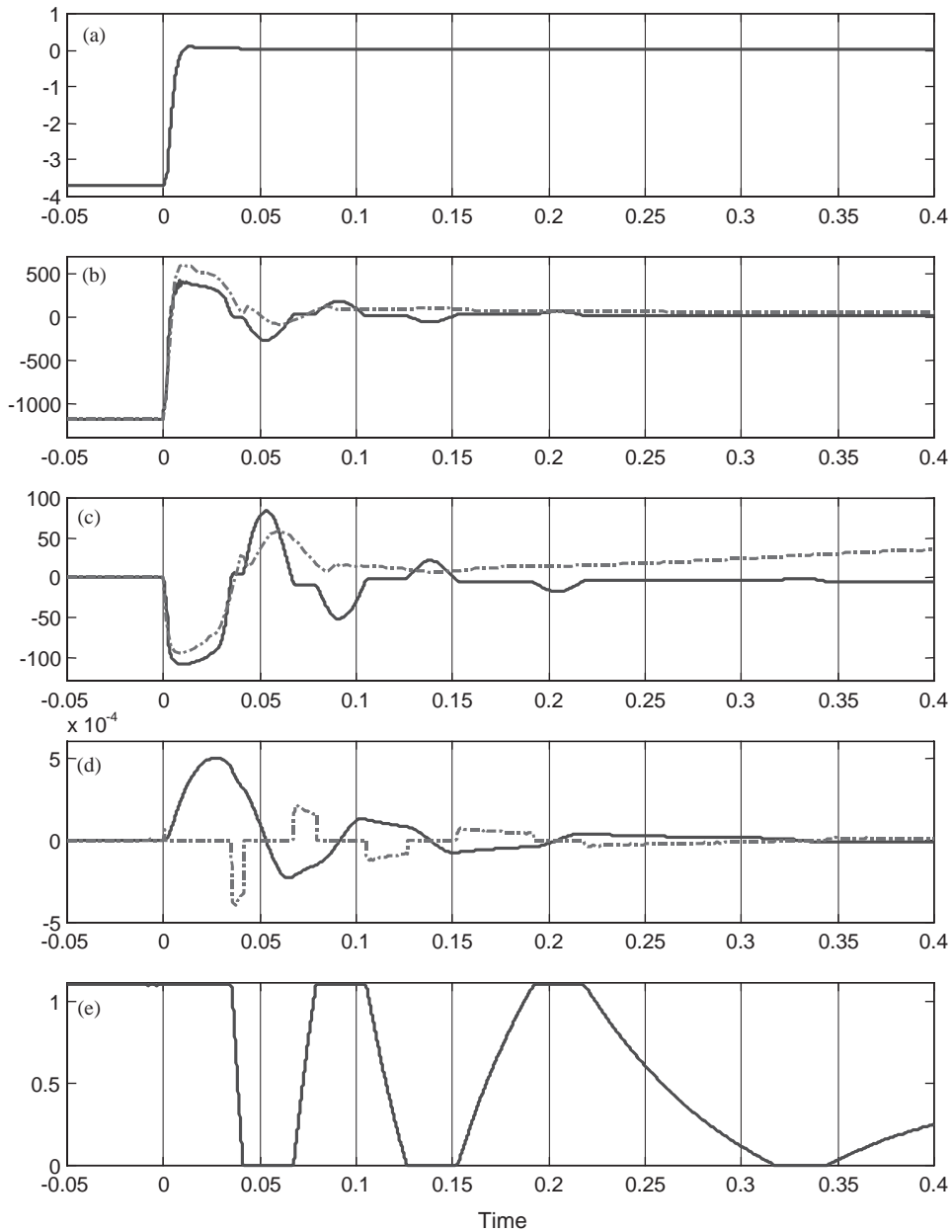
Fig. 22. Step response of the free decoupler mount. (a) Displacement excitation profile; (b) transmitted force: —, simulation; -·-·, measured; (c) upper chamber pressure; key: —, simulation; -·-·, measured; (d) flow through; key: —, inertia track; -·-·, decoupler; and (e) decoupler displacement.

For determining the inertance of the inertia track one-dimensional flow is assumed. Also, for estimating the resistance of inertia track a coefficient of discharge (with $C_d = 0.61$) is assumed for turbulent flow through an ideal sharp-edged orifice. The linear model of the decoupler is given by a
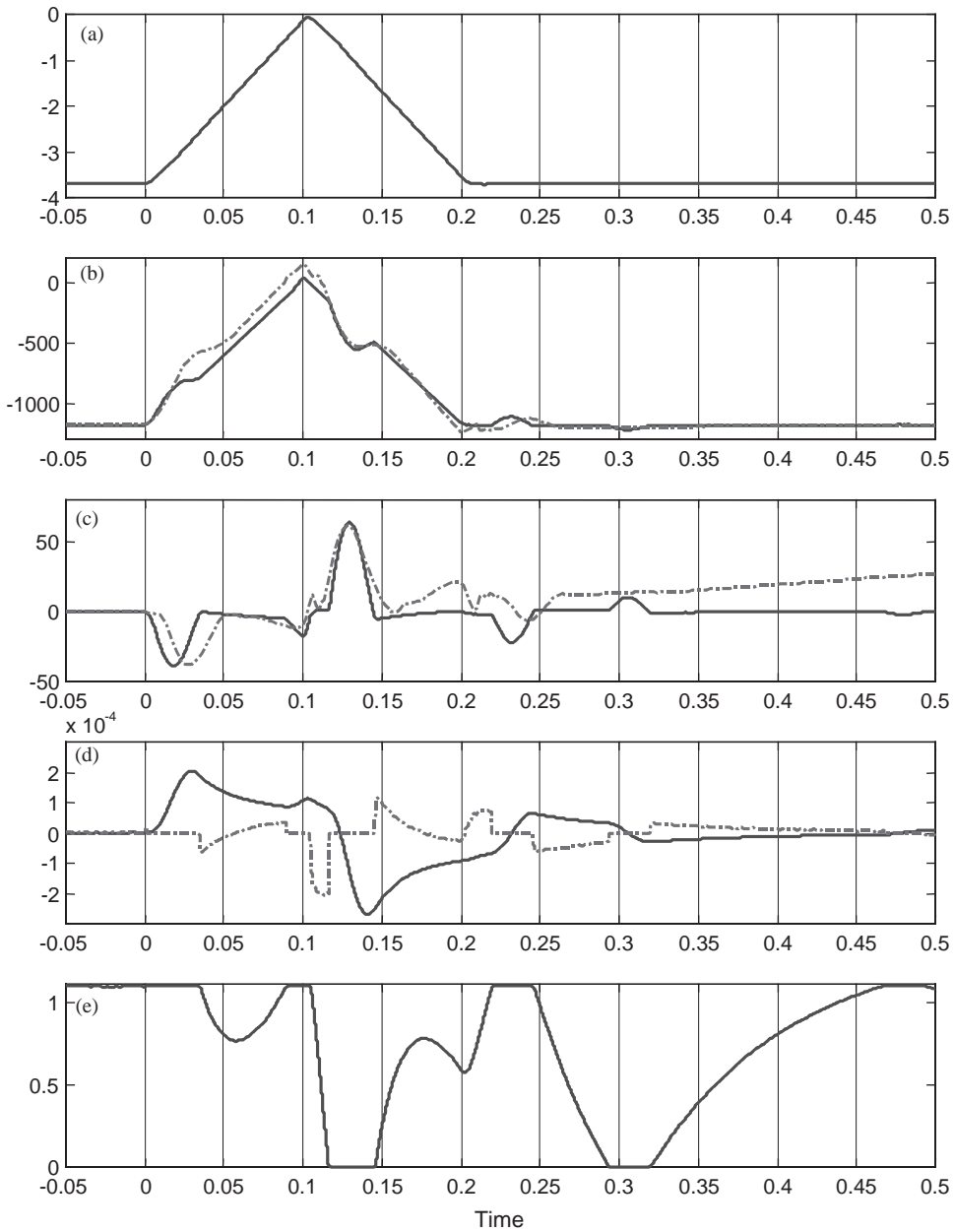
Fig. 23. Pulse response of the free decoupler mount. (a) displacement excitation profile; and (b) transmitted force: —, simulation; -·-·, measured; (c) upper chamber pressure; —, simulation; -·-·, measured; (d) flow through; —, inertia track; -·-·, decoupler; and (e) decoupler displacement.

first order differential equation with equivalent viscous damping though it is a combination of viscous and squeeze film damping elements. The compliant behavior of top chamber is assumed to be defined by a bi-linear spring but the transition from one stiffness regime to another is continuous.

Though this article reports new work on the transient response, we had to investigate the steady state behavior as well. Linear model based on transfer functions shows the effect of key parameters like the compliance of top chamber. The effect of vacuum formation on the overshoot for a step input is also observed by comparing measured data with linear model results. From the linear analysis, it is observed that the $K_{32}(s)$ transfer function, as given by Eq. (13), is capable of accurately predicting the dynamic stiffness and loss angle. Additionally, a non-linear model has been successfully developed that includes both continuous and discontinuous non-linear stiffness and damping formulations. Extensive simulations have been conducted in comparing alternate approaches to describe the decoupler mechanism. New dynamic experiments have also been conducted given step and pulse (triangle) displacement profiles. A new switching model of the decoupler based on an equivalent viscous damping mechanism concept is used and this formulation matches well with transient measurements. The proposed simulation model can also be integrated within a larger vehicle dynamic model.

Analysis of the steady state time domain data provides an estimation of the top chamber compliance under vacuum conditions, leading to an asymmetric stiffness characteristic. Time domain results for step input (up or down) also illustrate such all asymmetric behavior. This phenomenon needs to be better understood and modelled in future studies. Finally, the experimental procedure we have used could lead to a standard transient test and correlation method with real-life events.

Acknowledgements

References

[1] W.C. Flower, Understanding hydraulic mounts for improved vehicle noise, vibration and ride qualities, SAE Technical Paper 850975, 1985.
[2] G. Kim, R. Singh, Non-linear analysis of automotive hydraulic engine mount, American Society of Mechanical Engineers, Journal of Dynamic Systems, Measurement and Control 115 (1993) 482–487.
[3] G. Nessler, W. Stokes, R. Beikmann, J. Curtis, T. Mitchell, Roll-down process development for transmission garage shift quality, SAE Noise and Vibration Conference Paper 2001-01-1500, 2001.
[4] R. Singh, G. Kim, P.V. Ravindra, Linear analysis of automotive hydro-mechanical mount with emphasis on decoupler characteristics, Journal of Sound and Vibration 158 (2) (1992) 219–243.
[5] G. Kim, R. Singh, Study of passive and adaptive hydraulic engine mount systems with emphasis on non-linear characteristics, Journal of Sound and Vibration 179 (3) (1995) 427–453.
[6] J.E. Colgate, C.T. Chang, Y.C. Chiou, W.K. Liu, L.M. Keer, Modelling of a hydraulic engine mount focusing on response to sinusoidal and composite excitations, Journal of Sound and Vibration 184 (3) (1995) 503–528.
[7] T.J. Royston, R. Singh, Vibratory power flow through a non-linear path into a resonant receiver, Journal of Acoustical Society America 101 (4) (1997) 2059–2069.
[8] MTS System Corporation, Conversation with MTS, 2001.

 [9] S. Tewani, Personal Communication with Delphi Chassis, 2001–01.
[10] E.O. Doebelin, System Dynamics: Modeling Analysis, Simulation, Design, Marcel Dekker, New York, 1998.
[11] MTS Systems Corporation, TestStar II Control System Reference Manual, Minneapolis, MN, 1999.
[12] Mathworks, Inc., Learning SIMULINK version 3.0, Natick, MA, 1999.
[13] M. Tiwari, H. Adiguna, R. Singh, Experimental characterization of a non-linear hydraulic engine mount, Noise Control Engineering Journal (Jan./Feb.) (2003), in press.
[14] T.J. Royston, R. Singh, Study of non-linear hydraulic engine mounts focusing on decoupler modeling and design, SAE Technical Paper 971936, 1997.
[15] A. Cameron, Basic Lubrication Theory, Longman Group Ltd., Essex, UK, 1970.
[16] R.W. Fox, A.T. McDonald, Introduction to Fluid Mechanics, 4th Edition, Wiley, New York, 1992.